Chapter 8
Magnetic Force Microscopy for Magnetic Recording and Devices

Atsufumi Hirohata, Marjan Samiepour and Marco Corbetta

Abstract By coating a tip of a non-contacting scanning probe with a magnetic material, scanning probe microscopy can become sensitive to a stray field from the surface of magnetic materials and devices, magnetic force microscopy. The behaviour of such magnetic samples is well-known to be controlled by the formation and reversal of magnetic domains, each of which has a uniform magnetic moment separated by a region with moment rotation, a magnetic domain wall, to minimise total energy. The formation of the magnetic domains and walls is dependent upon size changes even at an atomic scale, which defines a critical length scale in much more strict manner than a semiconductor and metallic sample. It is therefore important to image magnetic domain structures of the magnetic samples precisely to reveal the corresponding performance. Magnetic force microscopy is one of the most convenient techniques for magnetic imaging with nanometric resolution as detailed in this chapter.

8.1 Introduction

In the development of new advanced magnetic materials and devices, it is critical to evaluate their properties not only in their bulk form but also in the form to be used, such as multilayered junctions, nanoparticles and nanocomposites. Recent progress in nanotechnology enables the production of atomically flat or abrupt interfaces in multi-layered junctions. The progress has been, for instance, allowed us to continue the increase in the number of transistors in a processor, as known as Moore's law. Similar increase has been achieved in the other electronic devices, such includes data storage and communication. However, we have not achieved uniform electron

A. Hirohata (✉) · M. Samiepour
Department of Electronic Engineering, University of York, Heslington, York YO10 5DD, UK
e-mail: atsufumi.hirohata@york.ac.uk

M. Samiepour
e-mail: marjan.samiepour@york.ac.uk

M. Corbetta
NanoScan AG, Überlandstrasse 129, Dübendorf 8600, Switzerland
e-mail: m.corbetta@nanoscan.ch

U. Celano (ed.), *Electrical Atomic Force Microscopy for Nanoelectronics*,
NanoScience and Technology, https://doi.org/10.1007/978-3-030-15612-1_8

transport across the entire interfacial area in such junctions due to the existence of local defects, which introduce differences in resistance. The defects are hence known to cause local heating and reduction in transport efficiency. To date, structural junction uniformity has been predominantly assessed by cross-sectional transmission electron microscopy (TEM) in atomic resolution. On the other hand, the corresponding imaging of magnetic information with similar atomic resolution is still under development.

8.1.1 Magnetic Imaging

The magnetic imaging has been achieved via interactions between a probe and magnetic fields (or magnetisation) of a specimen [1]. In the Bitter method, which is one of the most commonly used magnetic powder patterns, colloidal magnetite particles are used as a probe to form domain patterns due to the stray field from the sample surface. This is still an important method because of the simplicity and high sensitivity (~sub-micron resolution within a ~sub-micron subsurface region), however, it makes sample surface dirty.

For the deeper imaging, magneto-optical (MO) imaging can be used as listed in Fig. 8.1. MO effects, MO Faraday effect and Kerr effect (MOKE) can be used to observe magnetic domain configurations. Samples need to be flat and transparent for the Faraday effect observation. The MOKE also requires a flat surface but can measure local hysteresis and dynamic behaviour. These techniques can offer magnetic information up to about 20 nm (on metallic materials) below the surface with a resolution down to approximately 200 nm.

In order to improve the resolution of magnetic imaging, electron-beam and X-ray techniques have been used as an imaging probe. Among them, one of the most popular technique is Lorentz transmission electron microscopy (Lorentz TEM). In out-of-focus (defocused) mode, electrons are refracted within a sample due to the Lorentz force, and the interference contrast corresponds to the magnetisation distributions of the sample.

Using a similar TEM setting, electron holography can also be realized. The phase distributions of electrons transmitted through a specimen are recorded as an off-axis hologram using a collimated electron beam. The hologram can be reconstructed by using an interferometer [2].

On the other hand, using scanning electron microscopy (SEM), an electron beam (<10 keV) introduced perpendicular to the conductive sample generates secondary electrons, whose intensity corresponds to the stray field from the sample. Here, backscattered electrons can also be used for magnetic imaging.

Scanning electron microscopy with polarisation analysis (SEMPA) has also been used for high-resolution magnetic imaging. Since the secondary electrons from a sample are spin-polarised, these electrons are collected and measured as a normalised difference signal in a Mott detector. This method is sensitive to the surface magnetisation vector, and can be *in situ* [3].

By replacing electron-beam with X-ray, X-ray topography can be achieved. Aligning a slit to fulfil the Bragg condition with a monochromatic X-ray, the crystalline imperfection due to magnetostriction can be detected, *e.g.*, X-ray magnetic circular dichroism (XMCD) and X-ray photo-emission electron microscopy (XPEEM),

8.1.2 Magnetic Force Microscopy

In comparison to the above techniques listed in Sect. 8.1.1, magnetic force microscope (MFM) is one of scanning probe microscopes (SPMs) and is sensitive to a magnetic stray field from the sample (within 100 nm below the surface) by coating a tip for an atomic force microscope with a ferromagnetic layer. The development of MFM has started in 1980s, followed by the introduction of a commercial system in the early 1990. MFM is an easy method with the resolution better than ~10 nm without requiring any preparation for imaging among conventional magnetic imaging methods. This is why MFM has been widely used for magnetic imaging in fundamental research and device development. The details of the working principles and image examples will be described in Sects. 8.2 and 8.3, respectively.

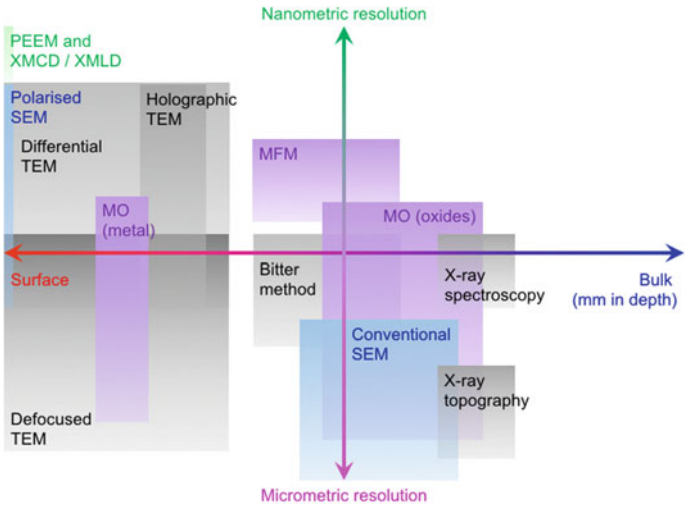

Fig. 8.1 Major techniques for the magnetic imaging against penetration depth of probes. After [1]

8.1.3 Other SPM-Based Magnetic Microscopy

8.1.3.1 Spin-Polarised Scanning Tunnelling Microscopy

Based on scanning tunnelling microscopy (STM) with a ferromagnetic tip, spin-polarised (SP-STM) has been developed. SP-STM was proposed in 1990 by Johnson and Clarke [4] and Wiesendanger et al. [5]. Spin-polarised secondary electrons can be generated using STM in the field-emission mode [6], which holds promise for nanoscale magnetic imaging. By comparing the signals of ferromagnetic (FM) and non-magnetic (NM) STM tips, atomic scale magnetic imaging can be achieved [5]. These reports were theoretically supported by Molotkov [7] and Laiho and Reittu [8] in 1993. This technique uses a direct-gap semiconductor tip. This is expected to be used to observe the surface magnetic configurations with an almost atomic resolution. Spin-polarised electron tunnelling from a Ni STM tip into a GaAs substrate was first demonstrated by Alvarado and Renaud [9]. The Ni tip is magnetised by an electromagnet and is used as a spin injector. It scans over the sample surface in its measurement state. Spin-polarised electron tunnelling through the vacuum is detected as circularly polarised EL signals in which the change is ~30% at room temperature (RT). This value corresponded to a minority electron spin polarisation of Ni(001) at the Fermi level. This suggests that minority spin electrons provide the dominant contribution to the tunnelling current.

After the first photoexcitation measurement by Prins et al. [10], modulated circularly polarised light has been used to excite spin-polarised electrons in a semiconductor (e.g., GaAs). Although optically excited electrons are scattered mainly at the semiconductor surface with back illumination [11], Sueoka et al. have demonstrated the possibility of detecting spin-polarised signals by scanning a Ni STM tip over a GaAs film with circularly polarised light shone through an AlGaAs membrane [12]. Suzuki et al. have performed a similar observation by scanning a *p*-GaAs STM tip over a Co film with back illumination through a mica/Au/Co film, and have obtained magnetic domain images [13]. GaAs tips are fabricated using photolithography and anisotropic etching to prevent limitations due to facets {105}. A three monolayer (ML) Co film exhibits perpendicular magnetisation and shows less than the magnetic circular dichroism (MCD) effect of 0.14%. This is much smaller than the observed polarisation response of about 10%. Polarisation modulation response images of the SP-STM show very good agreement with MFM images. In order to avoid the MCD effect and possible light scattering through the sample structures, Kodama et al. introduced photon helicity into a GaAs tip in the vicinity of the sample, which is equivalent of front illumination [14]. They detected a change of approximately 7% in Current-voltage (*I-V*) curves between right and left circular light irradiation of NiFe films.

8.1.3.2 Scanning Hall Probe Microscopy

A submicron Hall probe associated with precise STM positioning can be used to sense a stray field from a sample for scanning Hall probe microscopy (SHPM) [15]. This method is very sensitive to a magnetic field (~10e), however, it can be operated only at low temperature ($\leq$90 K). This technique can be used to detect a local perpendicular magnetic field from the surface of a sample [16]. The SHPM can also image magnetic induction under applied fields up to ~1 kOe and over a wide range of temperatures (a few 100 mK–300 K) which make this method suitable to study the effect of temperature on some phenomenon such as a domain wall structure in a ferromagnetic semiconductor and conventional vortex patterns on superconductors. In SHPM a nano-Hall probe with dimensions of ~50 nm $\times$ 20 nm has been fabricated by a combination of optical lithography and focused ion beam milling [17]. The probe is mounted on a piezoelectric tube (PZT) at a small angle with respect to the surface of a sample to minimise the distance between the probe and the sample surface during the measurement. By decreasing the distance between the Hall probe and the sample surface to 500–700 nm, the field resolution of the Hall can achieve 0.1Oe. The scanning area of a single image is between 14 $\times$ 14 (at 4 K) and 24 $\times$ 24 (at 30 K) μm^2 [18].

8.1.3.3 Scanning Superconducting Quantum Interference Device Microscopy

A superconducting quantum interference device (SQUID) can be used as a field detector. This SQUID microscopy is typically only valid at 4.2 K [19]. SQUID is a direct method to detect magnetic flux using a pick-up loop at low temperature (4 K). By measuring the magnetic flux in a mesoscopic ring, the current which is first derivative of the free energy of the ring dependent on the magnetic flux can be extracted as a fundamental thermodynamic property. SQUID is one of the most reliable instruments to measure a magnetic field. Traditionally the pick-up loop and SQUID sensor are used in flip-chip geometry. SQUID susceptometer has first been produced by Ketchen et al. [20]. The smallest current measured is reported to be 100 mA at 4.2 K. In 1993, a special SQUID technique has been developed where the sample and the SQUID sensor are patterned on the same chip [21]. The measured current of (4 ± 2) nA is comparable to the computed value of 5 nA in liquid Helium. In all these experiments, both the SQUID sensor and the sample are maintained at 4.2 K initially but only the sample is elevated up to room temperature. At room temperature, the sample has been separated from the SQUID loop with a thin window in a cryostat. Here, the spatial resolution plays an important role. In 2001, a German group has achieved a spatial resolution of $1\,pT/\sqrt{Hz}$ using a 50 μm thick sapphire window [22].

Furthermore, SQUID is a non-destructive technique which can also be used to detect the remanent magnetisation such as scratches, dents and mechanical stress in some stainless steels. A scanning SQUID susceptometer on a micrometric scale

objects has been reported in 2008 [23]. In this design, the pick-up loop (4 μm in diameter) and a modulation coil are separated to reduce cross coupling between them, allowing better coupling between the pick-up loop and the sample. The ability to isolate the sensor from the samples and background subtraction maximises the device utility and sensitivity. The completed model of the response of SQUID with sub-micron pick-up loops to different sources of magnetic fields has been calculated [24]. In this method, the coupling with London's and Maxwell's equations for a full geometry of measured magnetic flux is solved. The result of this calculation is in good agreement with experimental imaging with a deep sub-micron sized pick-up loop.

8.1.3.4 Scanning Near-Field Optical Microscopy

By introducing light through a submicron aperture, the diffraction limit of light can be circumvented, which provides an image 10–50 times better than a conventional optical image, known as scanning near-field optical microscopy (SNOM). Combining the SNOM with MOKE optics, both imaging and writing magnetic domains can be achieved [25]. SNOM is used to overcome diffraction in classical optical microscopy which limits spatial resolution. In SNOM, the excitation laser focuses in an aperture with diameter smaller than the excitation wavelength. The sample locates at small distance (near-field) below the aperture. The optical resolution is in the order of 30–50 nm [26]. This method made good progress on nanotechnology research, surface structures and bio-materials. By the microfabrication of SNOM probes, the resolution of the images can be better by a factor of 5–10 as compared with the classical microscopy [27]. Even though SNOM can achieve high-resolution imaging, SNOM requires challenging processes for the fabrication of the aperture since its pioneering demonstration in 1989. Fisher and Pohl have used the scattering of surface plasmons in a metallic film instead of aperture to image a sample in the near-field [28]. The main difficulty of this method is a very weak signal due to large illumination background and the influence of an extended part of tips other than just far extreme of the tip. One of reliable procedures is to use a single gold nanoparticle on very sharp glass fibre, achieving the resolution of an optical measurement of 100 nm [29]. A new magnetic microscope was introduced by a combination of SNOM and magneto-optical contrast which is called time-resolved near-field scanning magneto-optical microscope [30]. This microscope is used to study ultrafast magnetisation dynamics on sub-nanoseconds. J. Rudge et al. have measured a gyrotropic resonance frequency of vortex core in a micron-sized CoFeB disc at ~240 MHz. Recently, time-resolved scanning Kerr microscopy in the near-filed became one of intense methods to investigate magnetisation dynamics [31].

8.2 Principles of Non-contact/Tapping Mode

8.2.1 Principles of Non-contact Atomic Force Microscopy

Scanning probe microscopy (SPM) provides opportunities to obtain various kinds of information, such as height, magnetic pole and friction, using interactions between a probe and sample surface. As detailed in Chap. 1, the first SPM is scanning tunnelling microscopy (STM) invented by Binnig et al. [32]. By scanning a very sharp conducting tip in the vicinity of a sample surface with a bias application between the tip and the sample, a tunnelling current I_t can be detected as $I_t \sim V\exp(-Cd)$, where V is the bias voltage, C is a constant of the sample material and d is the distance between the lowest atom of the tip and the highest atom on the sample surface. Accordingly, I_t can be used in a feedback loop to control the precise movement of a piezoelectric scanner, which can be directly converted as topographic information. The ability of STM to measure surface morphology is clearly outstanding (atomic resolution). However, the most severe limitation is that both the tip and the sample must be almost perfect conductors.

In order to avoid the limitation in STM, Binnig et al. have invented atomic force microscopy (AFM) [33]. AFM also uses a very sharp tip for scanning over a sample but with a long cantilever with a low spring constant (~1 N/m). Since the tip senses interatomic force (van der Waals force), the cantilever is bent, the magnitude of which is detected as an electrical signal from a 2-segment photodiode using laser light reflection.

When the tip approaches the sample surface, the tip first feels the attractive force and is bent towards the sample surface. With further approach the sample surface, the tip encounters the repulsive force from the sample. At a certain distance these two forces are balanced, at which distance the AFM measures the topographical profile. One way of measuring the profile is to maintain the distance between the tip and the sample, and detect the amplitude of the force via the magnitude of the cantilever distortion (constant height mode). Another way is to keep the force constant, and measure the movement of the tip (constant force mode).

In AFM observation, well-known problems which one should be aware of are the large repulsive force from a contamination layer on the sample surface, the influence of statistic electronics from either the sample or the probe, and the friction between the sample and the tip during the AFM scan. To avoid such issues, Martin et al. have developed non-contact AFM (NC-AFM) [34]. When a probe resonating with small amplitude ($\ll$1 nm) is scanned 5–10 nm above the sample surface, the resonating frequency ω_0 shifts to ω_0' due to the atomic force F from the sample. If we take the sample plane normal as z axis, ω_0' is given by

$$\omega_0' = \omega_0\sqrt{1 - \frac{1}{k_z}\left(\frac{\partial F}{\partial z}\right)},$$

where k_z is the spring constant of the cantilever. In the Q-curve of the cantilever, a frequency ω_D^+, which satisfies

$$\omega_D^+ = \omega_0 \left(1 + \frac{1}{\sqrt{8Q}} \right).$$

ω_D^+ is typically used for non-contact AFM observation. This provides an amplitude shift of

$$\Delta A = \frac{2A_0 Q}{3\sqrt{3k_z}} \left(\frac{\partial F}{\partial z} \right).$$

When the probe is scanned as ΔA constant, topographical information can be obtained similarly to AFM. The resolution of NC-AFM typically depends upon the tip height from the sample, which is slightly less than that for contact AFM (5–10 nm [35]).

8.2.2 Principles of Magnetic Force Microscopy

With a magnetic tip magnetised in one direction, NC-AFM can become sensitive to magnetic force [36]. There are relationships between tip-sample distance z and force gradient $F' = \partial F / \partial z$ as shown in Fig. 8.2 [37]. In the distance range of $5 < z < 20$ nm, the tip mainly detects atomic force (van der Waals' force), while the tip is sensitive to magnetic force with $50 < z < 500$ nm. Magnetic force microscopy (MFM) senses magnetic force gradients from a sample due to the perpendicular component of the sample stray field. The cantilever is excited at its first longitudinal resonance (typically 50 kHz) and magnetic interaction with the surface is detected as shift of the resonance (typically of a few Hz, detected using phase-locked loop technology).

A magnetic probe, whose tip is magnetised perpendicular to sample surface, should be mounted on a tip holder. A schematic phase curve of the cantilever is shown in Fig. 8.3. The phase curve decreases with increasing frequency, and the 90° phase lag point (at the centre of the curve) corresponds to the peak frequency of the cantilever. The phase curve then measures the phase lag between the drive voltage and the cantilever response, and hence the vertical gradients in the magnetic force cause a shift ΔF_0 in the resonance frequency. This resonance shift ΔF_0 gives rise to a phase shift $\Delta\phi$, which provides an image of the magnetic force gradients (phase detection). Typically, phase detection is used to obtain MFM images because phase detection results are generally superior to those obtained with amplitude detection. Frequency modulation, which provides quantitative images of force gradients by directly detecting the drive frequency at 90° phase lag, can also be achieved. Further details about the tip-sample interactions can be found in [38]. The ΔF_0 also gives variations in oscillation amplitude ΔA, which can be used for imaging the magnetic force gradient (amplitude detection) (see Fig. 8.4 [39]).

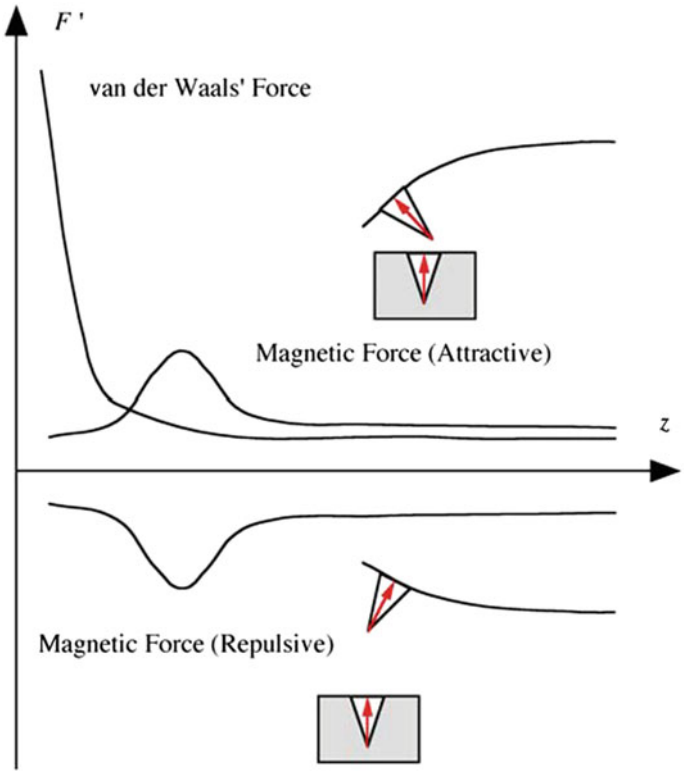

Fig. 8.2 Schematic energy diagram of force gradients for both van der Waals' and magnetic force

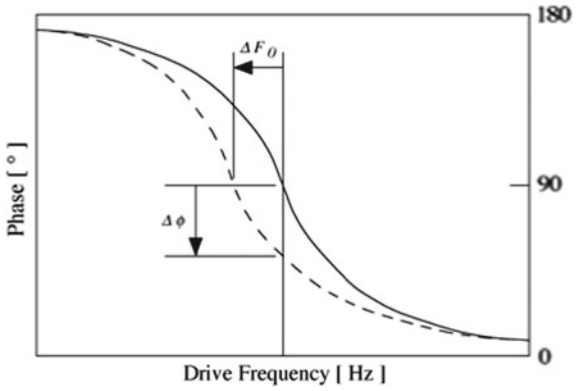

Fig. 8.3 Phase shift of a MFM cantilever at fixed drive frequency. After [39]

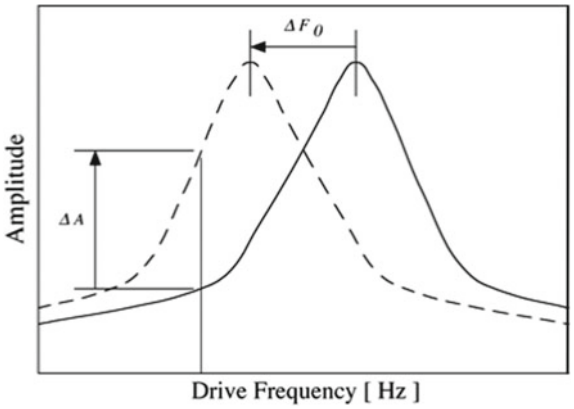

Fig. 8.4 Amplitude shift of a MFM cantilever at fixed drive frequency. After [39]

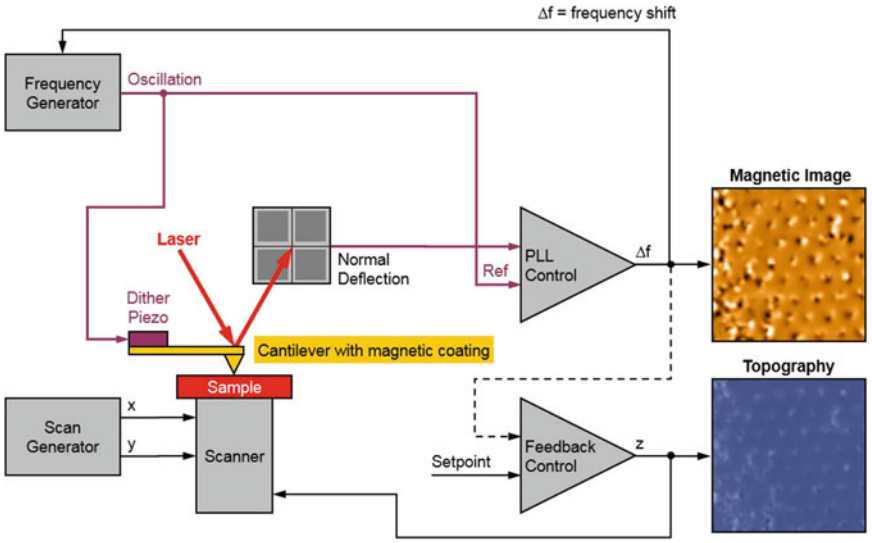

Fig. 8.5 Block diagram for MFM measurements

In MFM observation (see Fig. 8.5), a tapping cantilever first scans over the sample surface to obtain topographic information. Using lift mode as shown in Fig. 8.6, the tip is then raised just above the sample surface, where lift scan height h_{lift} is typically set as 100 nm unless samples have excessive surface height variations, and the surface topography is profiled while responding to magnetic influence on the same trace line.

In the lift mode, the total tip-sample distance h_{total} is the sum of the average tip-sample distance in the tapping mode h_{t} and the lift scan height h_{lift} as shown in Fig. 8.6. h_{t} is equal to the oscillation amplitude of the MFM cantilever, which is

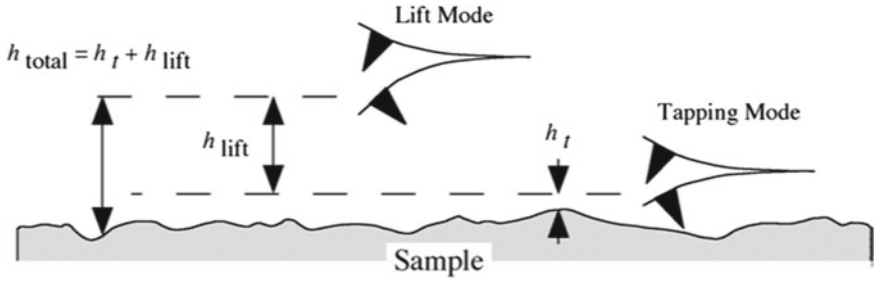

Fig. 8.6 Tip-sample distance and oscillation amplitude in both the tapping and the lift mode for MFM measurements

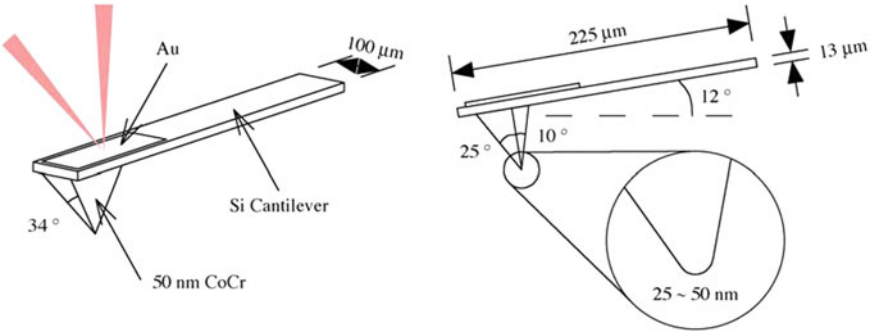

Fig. 8.7 Schematic views of typical magnetic force microscopy probe

determined by a setpoint. Typically, the setpoint of the measurements was chosen to be 1 V, which typically corresponds to h_t ~ 15–20 nm.

8.3 Magnetic Tips and Specifications

8.3.1 Magnetic Tips

Figure 8.7 shows schematics of a typical MFM probe. A standard etched Si probe with a CoCr coated tip is commonly used for MFM imaging. Specifications are listed in Table 8.1. The back of the cantilever has a reflective coating for better resolution. Here, the laser spot should be introduced around the centre of the cantilever to avoid optical interference.

In MFM, a Si-based cantilever is bent by attractive force between the different polarity, *i.e.*, between the N- and S-poles, and repulsive force between the same polarity, i.e., between the N- and N-poles or the S- and S-poles, occurring between the ferromagnetic tip located at the end of the cantilever and a stray field from

Table 8.1 List of commercial MFM tips

	Cantilever thickness (μm)	Cantilever width (μm)	Cantilever length (μm)	Force constant (N/m)	Resonance frequency (kHz)	Coating	Tip radius (nm)	Tip height (μm)	Coercivity (Oe)	Remanence magnetisation (emu/cm^3)	Effective magnetic moment (emu)	Imaging resolution (nm)
Bruker												
MESP	3 (2–3.5)	28 (23–33)	225 (200–250)	2.8 (1–5)	75 (50–100)	Co-Cr	35	10–15	~300		$\sim 10^{-13}$	
MESP-V2	2.80 (2.05–3.55)	35 (33–37)	225 (215–235)	3.0 (1.5–6.0)	75 (50–100)	Co-Cr	35	10–15	~300		$\sim 10^{-13}$	
Standard moment MFM probe with a conductive coating (MESP-CPMT)	2.75 (2–3.5)	28 (23–33)	225 (200–250)	2.8 (1–5)	75 (50–100)	Co-Cr	20	10–15	~400		$\sim 10^{-13}$	
High moment MFM probe (MESP-HM)	2.75 (2–3.5)	28 (23–33)	225 (200–250)	2.8 (1–5)	75 (50–100)	Co-Cr	80	10–15	~400		3×10^{-13}	

(continued)

Table 8.1 (continued)

	Cantilever thickness (μm)	Cantilever width (μm)	Cantilever length (μm)	Force constant (N/m)	Resonance frequency (kHz)	Coating	Tip radius (nm)	Tip height (μm)	Coercivity (Oe)	Remanence magnetisation (emu/cm^3)	Effective magnetic moment (emu)	Imaging resolution (nm)
High moment MFM probe (MESP-HM-V2)	2.80 (2.05–3.55)	35 (33–37)	225 (215–235)	3.0 (1.5–6.0)	75 (50–100)	Co-Cr	80	10–15	~300		~10^{-13}	
High moment MFM probe with a conductive coating (MESP-HMW)	2.75 (2–3.5)	28 (23–33)	225 (200–250)	2.8 (1–5)	75 (50–100)	Co-Cr	80	10–15	~400		~10^{-13}	
Low coercivity MFM probe with a conductive coating (MESP-LC)	2.75 (2–3.5)	28 (23–33)	225 (200–250)	2.8 (1–5)	75 (50–100)		35	10–15	<10		<10^{-13}	

(continued)

Table 8.1 (continued)

	Cantilever thickness (μm)	Cantilever width (μm)	Cantilever length (μm)	Force constant (N/m)	Resonance frequency (kHz)	Coating	Tip radius (nm)	Tip height (μm)	Coercivity (Oe)	Remanence magnetisation (emu/cm^3)	Effective magnetic moment (emu)	Imaging resolution (nm)
Low moment MFM probe with a conductive coating (MESP-LMW)	2.75 (2–3.5)	28 (23–33)	225 (200–250)	2.8 (1–5)	75 (50–100)		25	10–15	<400		3×10^{-14}	
MESP-LM-V2	2.80 (2.05–3.55)	35 (33–37)	225 (215–235)	3.0 (1.5–6.0)	75 (50–100)		25	10–15	<400		3×10^{-14}	
Nanosensor												
PointProbe® Plus Magnetic Force Microscopy Probe (PPP-MFMR)	3	28	225	2.8	75	Hard magnet	<50		~300	~300	$\sim 10^{-13}$	<50

(continued)

Table 8.1 (continued)

	Cantilever thickness (μm)	Cantilever width (μm)	Cantilever length (μm)	Force constant (N/m)	Resonance frequency (kHz)	Coating	Tip radius (nm)	Tip height (μm)	Coercivity (Oe)	Remanence magnetisation (emu/cm^3)	Effective magnetic moment (emu)	Imaging resolution (nm)
PointProbe® Plus Low Moment Magnetic Force Microscopy Probe (PPP-LM-MFMR)	3	28	225	2.8	75	Hard magnet	<30		~250	~150	1/2 of PPP-MFMR	<35
PointProbe® Plus Low Coercivity Magnetic Force Microscopy Probe (PPP-LC-MFMR)	3	28	225	2.8	75	Soft magnet	<30		~0.75	~225	3/4 of PPP-MFMR	<35

(continued)

Table 8.1 (continued)

	Cantilever thickness (μm)	Cantilever width (μm)	Cantilever length (μm)	Force constant (N/m)	Resonance frequency (kHz)	Coating	Tip radius (nm)	Tip height (μm)	Coercivity (Oe)	Remanence magnetisation (emu/cm^3)	Effective magnetic moment (emu)	Imaging resolution (nm)
SuperSharp SiliconTM High Resolution Magnetic Force Microscopy Probe (SSS-MFMR)	3	28	225	2.8	75	Hard magnet	<15		~125	~80	1/4 of PPP-MFMR	<25
MikroMasch												
High Quality (HQ): Magnetic Noncontact (NSC) silicon probe 18	3 ± 0.5	27.5 ± 3	225 ± 5	2.8 (12–5.5)	75 (60–90)	Co(60 nm)/Cr (20 nm)	<60	12–18	300–400			

(continued)

Table 8.1 (continued)

	Cantilever thickness (μm)	Cantilever width (μm)	Cantilever length (μm)	Force constant (N/m)	Resonance frequency (kHz)	Coating	Tip radius (nm)	Tip height (μm)	Coercivity (Oe)	Remanence magnetisation (emu/cm^3)	Effective magnetic moment (emu)	Imaging resolution (nm)
High Quality (HQ): Magnetic Noncontact (NSc) silicon probe 36	3 ± 0.5	32.5 ± 3	110 ± 5 90 ± 5 130 ± 5	1.0 (0.1–4.6) 2.0 (0.2–9.0) 0.6 (0.06–2.7)	90 (30–16) 130 (45–240) 65 (25–115)	Co(60 nm)/Cr (20 nm)			300–400			
NT-MDT												
High resolution long lifetime magnetic probe (MFM01)	2.5 ± 0.5	32 ± 5	225 ± 10	3 (1–5)	70 (47–90)	Co-Cr (30–40 nm)						20–30
Low Moment High Resolution Magnetic tip (MFM_LM)	2.5 ± 0.5	32 ± 5	225 ± 10	3 (1–5)	70 (47–90)	Co-Cr (15–20 nm)			~20			

(continued)

Table 8.1 (continued)

	Cantilever thickness (μm)	Cantilever width (μm)	Cantilever length (μm)	Force constant (N/m)	Resonance frequency (kHz)	Coating	Tip radius (nm)	Tip height (μm)	Coercivity (Oe)	Remanence magnetisation (emu/cm^3)	Effective magnetic moment (emu)	Imaging resolution (nm)
High Coercivity Magnetic Probe (MFM_HC)	2.5 ± 0.5	32 ± 5	225 ± 10	3 (1–5)	70 (47–90)	Co-Cr (~ 60 nm)			500–800 in vertical and >2 k in horizontal directions			
NanoWorld												
Magnetic force microscopy - reflex coating (MFMR)	3 (2.5–3.5)	28 (22.5–32.5)	225 (200–230)	2.8 (1.2–5.5)	75 (60–90)	Co alloy						
Soft magnetic coating - magnetic force microscopy - reflex coating (S-MFMR)	3 (2.5–3.5)	28 (22.5–32.5)	225 (200–230)	2.8 (1.2–5.5)	75 (60–90)	Soft magnet			~0.75	~225		

(continued)

Table 8.1 (continued)

	Cantilever thickness (μm)	Cantilever width (μm)	Cantilever length (μm)	Force constant (N/m)	Resonance frequency (kHz)	Coating	Tip radius (nm)	Tip height (μm)	Coercivity (Oe)	Remanence magnetisation (emu/cm^3)	Effective magnetic moment (emu)	Imaging resolution (nm)
Team Nanotec												
High resolution magnetic probe tip (ML 1)				3.0 or 0.7	75 or 45	~20 nm thick Co-alloy hard magnet	15	>9				
High resolution magnetic probe tip (ML 3)				3.0 or 0.7	75 or 45	~37 nm thick Co-alloy hard magnet	20	>9				

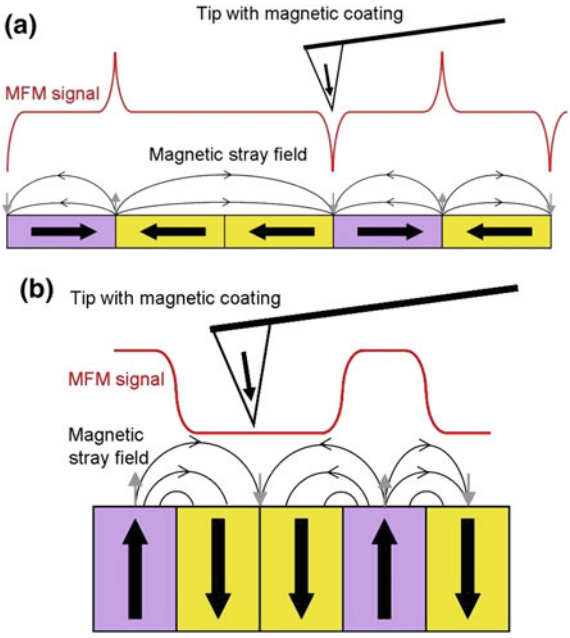

Fig. 8.8 Principle of magnetic force microscopy over a sample surface with **a** in-plane and **b** perpendicular magnetisation. The magnetically-coated tip detects the vertical component of the stray field (grey arrows) emanating from the surface. Hence, the MFM signal (in red) exhibits peaks at the domain boundaries

a specimen. The tip has the height of ~10 μm with the curvature of 25–50 nm, which is coated by 10–100 nm thick ferromagnetic layers, *e.g.*, CoCrPt and CoTa, as detailed in Sect. 8.2. By detecting the displacement of the cantilever by the attractive and repulsive force via a photodetector, magnetic imaging can be achieved. Here, the force F between the MFM tip with the magnetisation m and the stray field from the specimen H can be defined as $F = \nabla(m \cdot H)$. By directly detecting the force, static MFM can be achieved, which is relevant for a large stray field (>6 kOe [40]) from a specimen, e.g., bulk permanent magnets. However, a stray field from a thin-film device (<2 Oe [40]), such as hard disk media and magnetic memory, is too small to be detected. Hence, dynamic MFM has been developed by vibrating the cantilever perpendicular to the specimen plane to detect changes in the amplitude, phase and frequency of the vibration as described in Sect. 8.2.2. Here, the gradient of a magnetic force ∇F_z from an in-plane magnetised specimen is detected as shown in Fig. 8.8a. As shown in Fig. 8.8a, the MFM signals are reversed depending on the attractive and repulsive force. For the case of perpendicularly magnetised specimen, the representative schematics are shown in Fig. 8.8b.

In MFM images, brighter contrast means positive frequency shift which in turn depicts repulsive interaction or a magnetic stray field of the surface anti-parallel to the magnetisation of the tip. Darker contrast translates as negative frequency shift, or attractive interaction and a magnetic stray field of the surface parallel to the tip magnetisation.

8.3.2 Improvement of Specifications

Magnetic imaging is performed by detecting displacement of Si-based cantilever with a MFM tip coated with a ferromagnetic layer [41–46]. In order to increase the imaging resolution, the distance between the MFM tip and the specimen needs to be closer but it increases the contributions from the specimen topology. Hence, for the high-resolution imaging, a sharper tip [43–47] and improvement of the field gradient [45, 46] are necessary. As listed in Table 8.1, commercial MFM tips have their resolution of 20–40 nm, which requires further improvement for high-density recording media. In addition, for highly anisotropic recording media and permanent magnets, the magnetisation of the MFM tip is affected by the stray fields from these specimens [48]. It is therefore essential to achieve both high resolution and high coercivity for imaging [49, 50], requiring a highly anisotropic material as a ferromagnetic coating layer on the MFM tip.

By introducing an alternative magnetic field to a ferromagnetic nanoparticle attached on a MFM tip, alternating magnetic force microscopy (A-MFM) has been developed with higher resolution. The alternative field has a frequency different from the resonant frequency of the cantilever, so that alternating gradient field can be generated by the nanoparticle, which can be detected from the highly coercive MFM tip independently. This method is sensitive to a stray field near the specimen surface with the resolution better than 10 nm [51].

8.4 Applications for Magnetic Recording

Since the 1970s, commercial mass data storage has been available with continuously diminishing costs and increasing storage capacity. The old eight-inch floppy disk displayed a storage capacity of 250 kB, which today might seem like an incredibly low capacity, however large-scale production was a technological prowess back then.

From the first floppies to the currently available terabyte hard disk drives (HDDs), the principle of data storage continues to be the same: the active component is a magnetic layer that stores information in the form of 0 s and 1 s by being magnetised locally in one direction or its opposite. The layer is placed on a spinning disk that can be written and read by a mobile head.

One remarkable progress in magnetic media recording was accomplished with the discovery of the Giant Magnetoresistance effect (GMR) by Albert Fert and Peter Grünberg, which got him the Nobel Prize in 2007. This effect facilitated moving from in-plane magnetic media recording to perpendicular media recording (PMR), thus expanding the storage capacities by over three orders of magnitude. Technologists today are discovering new tricks to improve density and pack more terabytes in hard disks measuring just a couple of inches wide.

Fig. 8.9 Photograph of a floppy disk

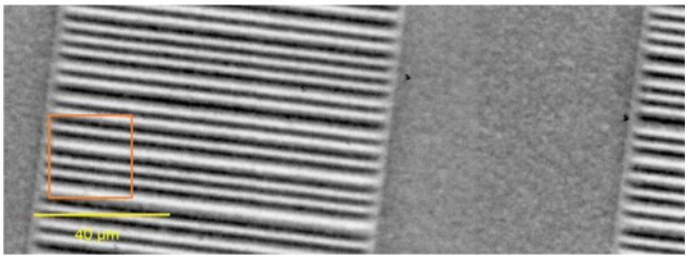

Fig. 8.10 75 × 200 μm^2 MFM image of a floppy disk. Magnetisation is in-plane, contrast arises from the magnetic stray field at the domain boundaries. The orange square illustrates the dimensions of Fig. 8.12 (25 × 25 μm^2 MFM image of a zip drive)

8.4.1 3.5-in. Floppy Disk Introduced in 1987

In the 1970s, magnetic storage made its appearance and a decade later became a widespread consumer good (Fig. 8.9). The bits of an 8 in. floppy disk were macroscopic so that they can hardly be imaged with an MFM. Since 1987, the next-generation floppies, the 3.5-in. disks, already had bits that had shrunk to a microscopic 2 × 100 μm^2, as shown in the MFM image as shown in Fig. 8.10.

Here, magnetisation in this case is oriented in the plane of the layer and hence the MFM detects the vertical magnetic stray field originating at domain boundaries, as shown in Fig. 8.8a.

The floppy disk shown here is a "High Density" disk with 1.44 MBytes of storage, or 11.52 Mbits (1 Byte = 8 bits) dispatched on a 3.5 in. platter. Taking into consideration the one-inch rotor, that makes an area of 8.84 $in.^2$ of active layer. However, not the entire area is available for data storage: for example the rims of the disk cannot be written and formatting also occupies space. Counting the bits in the 75 × 200 μm^2 MFM image (approximately 37 bits), a density of 1.6 Mbit/$in.^2$ can be established. Thus, 7.2 $in.^2$ or 81% of the whole surface is requested to store 11.52 Mbits of infor-

Fig. 8.11 Photograph of a zip disk

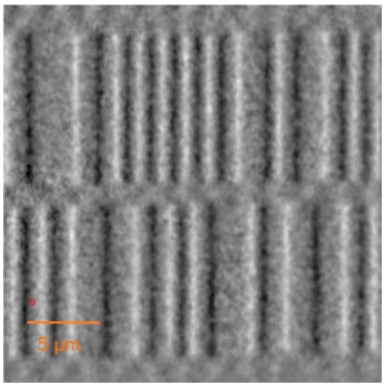

Fig. 8.12 $25 \times 25\ \mu m^2$ MFM image of a zip drive. Magnetisation is again in-plane. The red square illustrates the scale of Figs. 8.14, 8.15, 8.16 and 8.17 ($500 \times 500\ nm^2$ MFM image of HDDs)

mation. This leads to the areal density of 1.6 Mbit/in.^{2}, to put the number to scale with the following Hard Disk Drives that is a density of 0.0016 Gbit/in^2.

8.4.2 Zip Drive Introduced in 1994

After the arrival of the floppy disk, the zip drive was introduced in 1994. The size of the medium was still a 3.5 in. platter, and magnetic information was still stored in-plane, but due to its decreased bit size, the storage capacity could be expanded to 100 MB or 800 Mbits (Fig. 8.11).

In Fig. 8.12 showing a MFM image of $25 \times 25\ \mu m^2$, the bit dimension is assessed to be $1 \times 10\ \mu m^2$, which is 20 times smaller than in the floppy disk.

On the MFM data, 54 bits are counted, amounting to a density of 56 Mbit/in.^{2}, which makes 403 Mbits on the available 7.2 in.^{2} (assuming the same active area as on a floppy disk) or approximately 800 Mbits when considering both faces of the

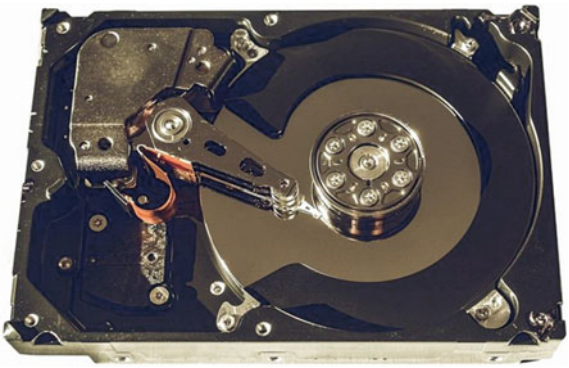

Fig. 8.13 Photograph of HDD

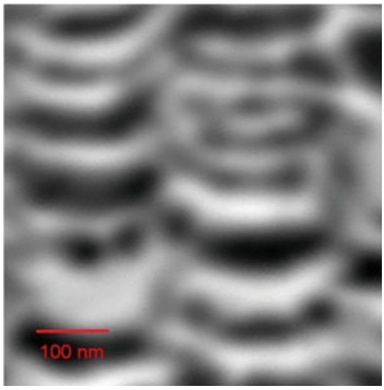

Fig. 8.14 500×500 nm^2 MFM image of a Fujitsu HDD from 2007. Magnetisation is perpendicular to the surface

zip. This figure is in seamless agreement with the Manufacturer's specifications. This leads to the areal density of 56 Mbit/in.^{2}, that is just 0.0056 Gbit/in.^{2}.

8.4.3 Fujitsu HDD Introduced in 2007

After the discovery of the GMR effect, the bits could be written vertically in the medium and much more information could be packed into the same area. From the early 2000s onwards, Perpendicular Magnetic Recording (PMR) became the norm and Hard Disk Drives were launched (Fig. 8.13).

The following 500×500 nm^2 MFM image was captured on a Fujitsu HDD from 2007 comprising of a single 2.5 in. platter and stipulating a total storage capacity of 40 GB or 320 Gbits. The bit dimension derived from the image is approximately 25×200 nm^2 which makes it 2000 times smaller than in a zip drive. Logically, the density also makes a massive leap: on average 37.4 bits are counted on this MFM data, on an area of only 0.25 μm^2: that comprises a density of 100 Gbit/in.^{2}.

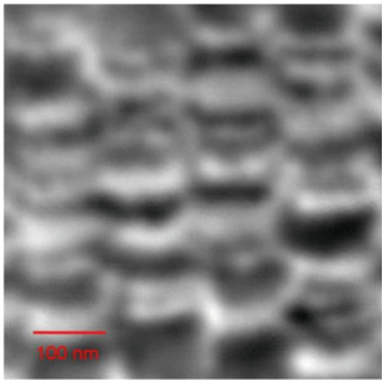

Fig. 8.15 $500 \times 500\ \text{nm}^2$ MFM image of a Seagate HDD from 2009

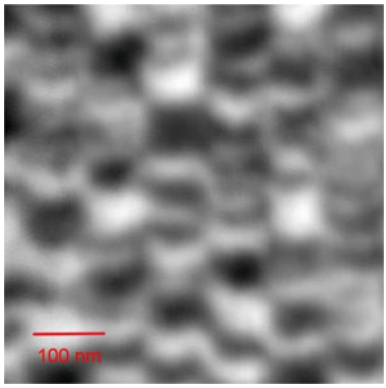

Fig. 8.16 $500 \times 500\ \text{nm}^2$ MFM image of a Western Digital HDD from 2012

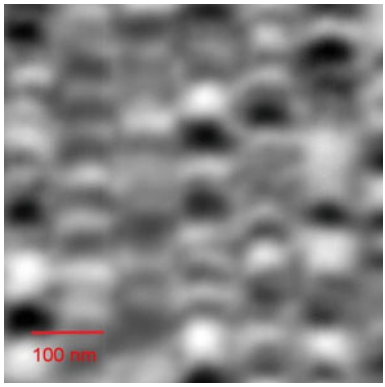

Fig. 8.17 $500 \times 500\ \text{nm}^2$ MFM image of a Seagate HDD from 2016

8.4.4 Seagate HDD Introduced in 2009

Since then, the race for ever-shrinking bits was propelled. In the spring of 2009, Seagate commercialized a Hard Disk Drive totaling 500 GB (4000 Gbits or 4 Terabits) split on two 2.5 in. platters.

The 500 × 500 nm^2 MFM image above represents 83.2 bits on average, the bit sizes amounts to ca. 20 × 125 nm^2. This signifies a gain of over a factor of two in bit size over the Fujitsu HDD. Logically, the bit density increases to 215 Gbit/$in.^2$.

8.4.5 Western Digital HDD Introduced in 2012

In 2012, Western Digital commercialized a HDD that had 1 TB or 8 Tbits of storage capacity divided over two 2.5 in. platters. The 500 × 500 nm^2 MFM image below displays 190 bits on average, the bit sizes totals to ca. 17 × 80 nm^2, which is becoming hard for an MFM to image. The bit area represents again a gain of over a factor of two in bit size over the earlier Seagate HDD, the bit density increasing to 490 Gbit/$in.^2$.

8.4.6 Seagate HDD Introduced in 2016

Since 2015, the battle for bit size reduction became harder as the physical limitations to the stability of the bits were increasingly reached. HDD Manufacturers have examined two tricks as workarounds in the existing Perpendicular Magnetic Recording technology. Both have the objective of reducing the width of the bits:

- Shingled Magnetic Recording (SMR): similar to roof tiles, a track is written overlapping the earlier neighbouring track.
- Two-Dimensional Magnetic Recording (TDMR): so as to prevent inter-track interference during readout of very narrow tracks, an array of read-heads is used to read adjacent tracks and correlate data. This technology, combined to SMR would gain another 5–10% of storage capacity.

The HDD from Seagate illustrated below is from the BarraCuda series (up to 5 TB of storage on three 2.5 in. platters) and according to the Manufacturer employs the SMR technology. However, from the MFM image, only a weak increase of storage density can be noticed. The 500 × 500 nm^2 MFM image below displays 208 bits on average, the bit size amounts to ca. 16 × 77 nm^2: compared to the earlier Western Digital HDD there is only a minor improvement of the bit size of a factor of 1.1. The bit density is 540 Gbit/$in.^2$.

Both TDMR and SMR technologies are thought to be stop-gap measures where read heads can be made smaller but write heads not. Moreover, SMR highlights the issue of re-writing a track, which has an incidence on the following adjacent tracks.

8.4.7 Outlook

Beating the 1 Tbit/in^2 limit is the next challenge HDD Manufacturers are currently facing. Bear in mind: a storage density of 1 Tbit/in^2, that is a bit size of just 12.7 $\times$ 50 nm^2.

The active layer of present day HDDs is made up of magnetic grains (usually CoPtCr alloys) clustered together, with dimensions of just few nanometers, typically 8 nm. The actual bit size is so small that less than 20 grains make up each bit.

Intuitively, to expand capacity it would be enough to reduce additional bit size and hence have fewer grains composing a bit. But this would weaken the Signal-to-Noise ratio and would make readout more complex.

Alternatively, one could think of decreasing the grain size. However physics stalls this: a smaller grain cannot hold its magnetisation anymore as thermal activation at room temperature will serve to flip its spin.

However, there are technological solutions, which are currently under investigation. One possible technology enabler would be to employ other alloys with higher anisotropy and hence greater thermal stability. The downside to it is that writing would become a lot more laborious and would require to local energy introduction, such as heat and microwave, onto the active layer to provisionally lower the magnetisation barrier. This so-called heat-assisted magnetic recording (HAMR) [52, 53] and microwave-assisted magnetic recording (MAMR) [54] would hence not only need new materials but also new and intricate read/write heads.

In HAMR, a laser beam is employed to heat the media up locally and reduce the thermal stability of the data bit to be written. A scanning near-field optical microscope is implemented into a writing head and a successful demonstration has been reported [55]. In 2012, TDK demonstrated a new HAMR head with the areal density of 1.5 Tbit/in.^{2} and bit-error rate of 10^{-2}. Seagate also demonstrated a new HAMR drive in 2012. HAMR contains many properties, such as grain size, characterisation and optimisation of a laser unit, media thermal stack and magnetic distributions. The optimisation of these properties can improve the density of HAMR and can reduce the corresponding energy consumption. In 2015, Seagate demonstrated a HDD using the HAMR technology by laser pulse instead of continuous wave [56]. Fruchart et al. have suggested the utilisation of thermal gradients generated in HAMR can determine the polarisation of tunnelling electrons across the media grain boundaries [57]. Matlak and Komvopoulos have reported a role of pulsed substrate bias voltage and a C^+ ion incident angle as well as the thickness of 1–4 nm thick amorphous C films deposited by filtered cathodic vacuum arc deposition method (FCVA) [58]. They show FCVA can produce extremely thin and uniform protective *a*-C films with high sp^3 contents ideal for HAMR heads.

Microwave-assisted magnetic recording (MAMR) was proposed by Zhu et al. [54]. The MAMR utilizes microwaves to reduce the switching field by an order of magnitude [59]. Western Digital announced that they will introduce a MAMR system within a few years. Instead of a conventional one-dimensional transverse microwave field, an ac field with a circular trace can increase efficiently of MAMR [60]. By

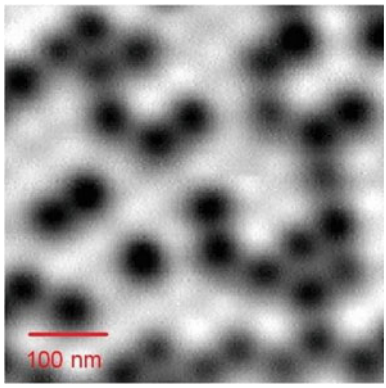

Fig. 8.18 500×500 nm^2 MFM image of a BPM. Sample courtesy of Seagate

utilising a circular ac field, a damping constant increases by an order of magnitude as compared with a linear ac field which achieves the areal density of 1.9 Tbit/in.^{2}. Following the utilisation of a circular ac field in MAMR a new micromagnetic modelling on MAMR shows the areal recording density can exceed 3 Tbit/in.^{2} with medium signal-to-noise and thermal stability at $K_u V = 60 k_B T_{300K}$. This model uses a perpendicular spin oscillator (PSTO) to generate localised a circular ac field [61]. Muraoka et al. have showed a stable spin torque oscillator (STO) requires a large and well-shaped gap field [62].

Another solution that can be considered is to pattern the active layer so as to physically define the shape of the storage unit: these are called bit-patterned media (BPM) [63] and are also under investigation as shown in Fig. 8.18. By patterning nano-scale island-shaped bits typically consisting of 10–20 grains, the media can achieve 10 Tbit in.$^{-2}$. Production of the layers would then need additional steps, which is a huge disadvantage in keeping production costs low. According to a recent calculation model, the areal density can even achieve beyond 10 Tbit/in.^{2} with a grain size of 5 nm in diameter and 10 nm in height [64]. As Advanced Technology Consortium reported that by utilising BPM in HAMR, the areal density can lead to 10 Tbit/in.^{2} by 2025. Nano-imprint lithography is suggested to use for high-density data storage applications. In BPM, the metallopolymer precursor is used as photoresist, which can be imprinted on the substrate [65].

In Fig. 8.18, there are on average 92.5 dots over an area of 500×500 nm^2 which makes a density of just 240 Gbit/in^2. The pitch between each dot is 50 nm in this sample from 2009. To realise a density of 1 Tbit/in.^{2}, the pitch between each dot would have to be halved to 25 nm.

HAMR, MAMR, BPM, or a combination thereof: in the days to come it will be known which path technologists have chosen to take to solve the challenge of data storage capacity. The Advanced Storage Technology Consortium (ASTC) roadmap, issued by the International Disk Drive Equipment and Materials Association (IDEMA) provides a hint of what is anticipated in the next 10–15 years (Fig. 8.19).

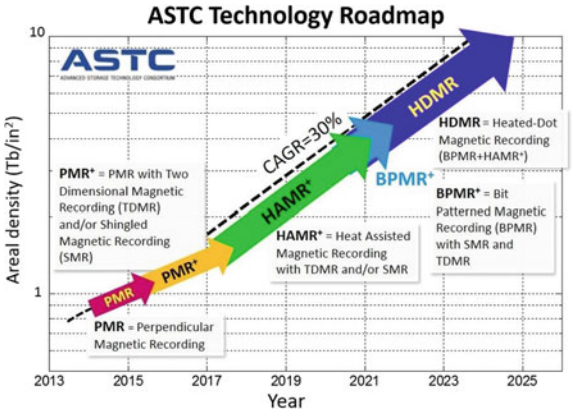

Fig. 8.19 ASTC Technology Roadmap gives an insight of the evolution of storage density in the coming 5–10 years in relation with the development of new technologies [66]

8.5 Applications for Magnetic Memories and Devices

8.5.1 Magnetic Random Access Memory and Spin Random Access Memory

After the commercial success of the HDD heads and media as described in Sect. 8.4, one of the major ongoing device studies is to realise a magnetic random access memory (MRAM) and/or spin random access memory (SpinRAM) [67]. MRAM can achieve the following features [68]: (i) non-volatility similar to HDD without using a mechanical head, (ii) read and write times of the order of nano-seconds, (iii) high density and (iv) low-power consumption. Hence, MRAM/SpinRAM is a good candidate for a universal memory. MRAM/SpinRAM can also avoid the delay and unnecessary power consumption due to circuit leads, and can provide a high-density circuit by the converting passive current leads in conventional electronic devices into memory cells.

For the next-generation MRAM/SpinRAM, the following issues need to be solved: the reduction of the switching field or critical current density and a reduction of the fabrication rule. Based on the scalability of MRAM/Spin RAM bits, spin-transfer torque (STT) must be used as discussed above. For the reduction of power consumption, the thermal stability of the free layer has to be compromised. A synthetic ferromagnet, such as CoFeB/Ru/CoFeB, has been implemented as the free layer by AIST [69], resulting in a five times increase in thermal stability with only an 80% increase in the critical current density. This configuration can achieve a 10 Gbit SpinRAM device. The remaining issue to realize a high-density SpinRAM is the reduction of the fabrication rule, which may be achieved by replacing the additional transistor with a possible new device design.

For the design improvement, MFM imaging can play an important role to remove any edge domains and magnetic defects to minimise the corresponding magnetisation

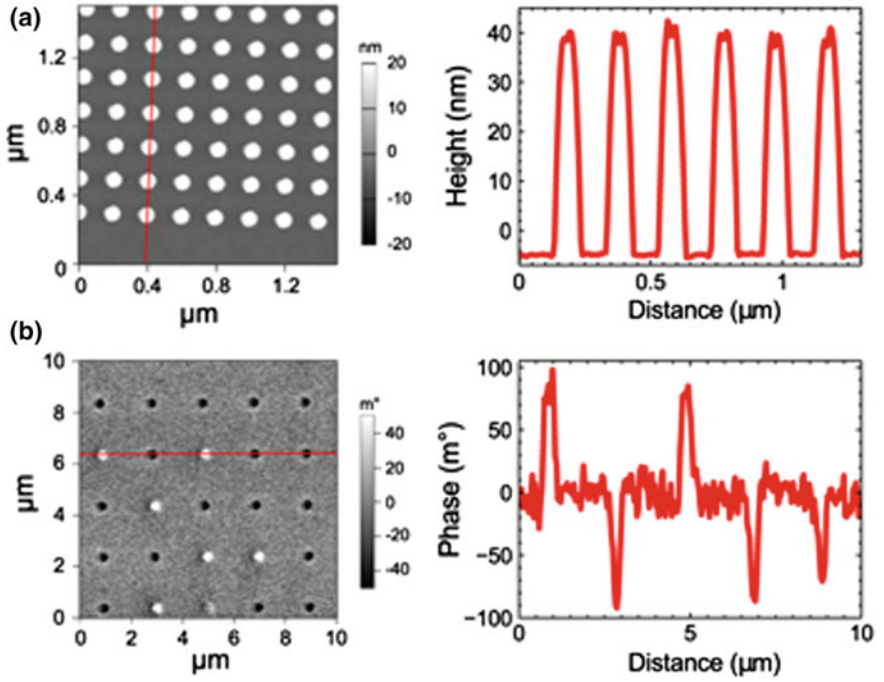

Fig. 8.20 **a** MFM topography image of patterned Mo/CoFeB/MgO/CoFeB/Mo p-MTJ pillars of 125 nm in diameter and **b** phase images from the magnetic structure of the same sample of p-MTJ pillars of 500 nm in diameter, representing the pillars after out-of-plane ac-demagnetisation [70]

damping. MFM was used for imaging perpendicular magnetic tunnel junction (p-MTJ) pillars after ac-demagnetisation in a perpendicular field [70]. Figure 8.20a, b show AFM topography and corresponding MFM images of an array of pillars made from a Mo/CoFeB/MgO/CoFeB/Mo film. The topography shows a uniform set of pillars with height of about 40–50 nm, corresponding to the thickness of the Mo/CoFeB/MgO/CoFeB/Mo/Ru. As shown in Fig. 8.20b, the ac-demagnetisation generates up and down magnetisation of the ferromagnetic layers in p-MTJ. The images for 500 nm pillars sizes show single domain structure even at this large size.

8.5.2 Racetrack Memory

In order to minimize the total magnetic energy of a ferromagnetic structure, a domain wall (DW) with a width of the order of 100 nm can be formed between magnetic domains. The competition among the energy terms, magnetostatic, exchange and anisotropy, produces magnetic domains, mainly due to the magnetostatic energy in a

mesoscopic ferromagnet. Within a DW, the spins gradually rotate from the direction of the domain to the direction in the neighbouring domain. If the ferromagnet is thick, the spin rotation within the wall is out-of-plane, forming a Bloch wall. For thin ferromagnet films, in-plane rotation, known as a Néel wall, occurs. For an intermediate ferromagnetic film thickness, a combination of these two walls, a cross-tie wall, forms [71].

Following Slonczewski and Berger [72, 73], STT has also been applied to displace a DW by flowing an electrical current (see Fig. 8.21). A ferromagnetic micro-wire has been prepared with a DW, giving a current density between 10^{11} and 10^{12} A/m^2 for wall motion [74, 75]. The velocity of the wall motion has also been estimated to be 2–6 m/s [76]. A similar experiment has also been performed in a dilute magnetic semiconducting wire [77].

8.5.3 Magnetic Skyrmion Logics

A similar concept to Sect. 8.5.2 was demonstrated by employing a magnetic skyrmion [78] and magnon [79] instead of a DW, which are expected to warrant reproducible motion by a lower current density as compared with the studies described as above. A magnetic skyrmion is a topologically protected structure by forming a rotating structure of spins. Depending on the rotating structure, the skyrmions can be categorised into three types, Néel, Bloch and anti-skyrmions. They have these chirality and the polarity of the centre spin, which can be used as information carrier. Due to the diameter of the skyrmion (typically ~10 nm), the corresponding critical current density can be reduced by five orders of magnitude.

The displacement of a magnetic skyrmion can also be imaged using MFM [80]. In Fig. 8.22, the velocity of the skyrmion generated on the Pt (5 nm)/FM/Au (3 nm)/FM/Pt (5 nm) multilayer, where FM = Ni (0.4 nm)/Co (0.7 nm)/Ni (0.4 nm), was measured by applying a 3-ns-long current pulses with a density of $j = 3.9 \times 10^{11}$ A/m^2. Under a magnetic field application of −60 Oe, the velocity was measured to be 60 m/s.

These results unambiguously confirm the importance of MFM imaging for the development of magnetic and spintronic devices. Due to the easy use of MFM, it can be utilised in broader fields in research and development.

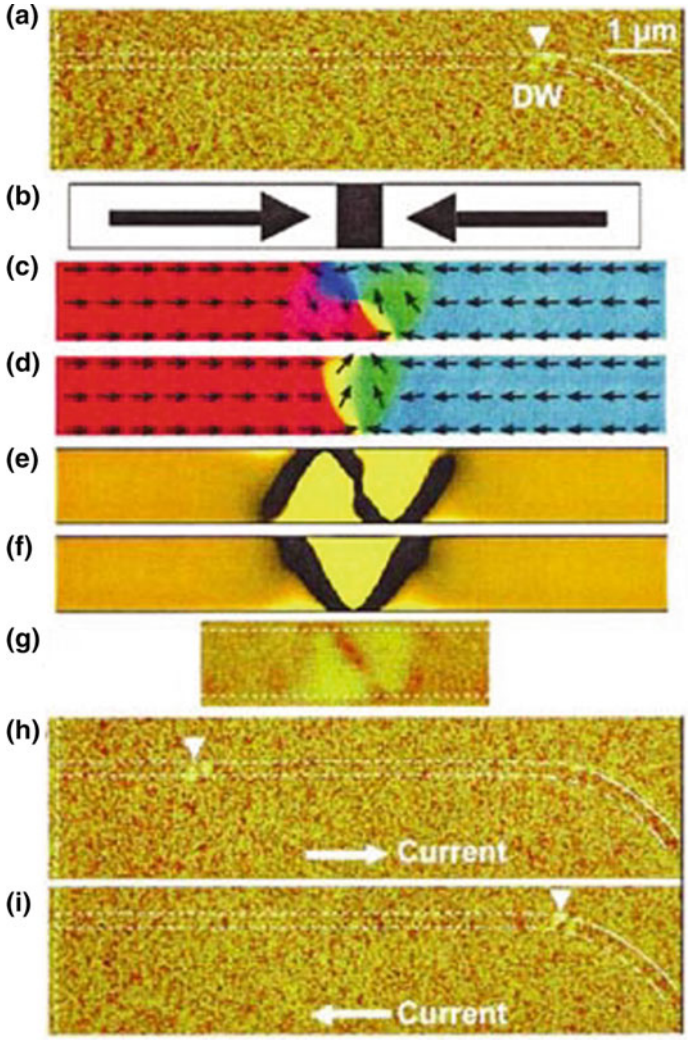

Fig. 8.21 **a** MFM image after the introduction of a DW. DW is imaged as a bright contrast, which corresponds to the stray field from positive magnetic charge. **b** Schematic illustration of a magnetic domain structure inferred from the MFM image. DW has a head-to-head structure. **c** Result of micromagnetics simulation (vortex DW). **d** Result of micromagnetics simulation (transverse DW). **e** MFM image calculated from the magnetic structure shown in (**c**). **f** MFM image calculated from the magnetic structure shown in (**d**). **g** Magnified MFM image of a DW. **h** MFM image after an application of a pulsed current from left to right. The current density and pulse duration are 1.2×10^{12} A/m^2 and 5 μs, respectively. DW is displaced from right to left by the pulsed current. (i) MFM image after an application of a pulsed current from right to left. The current density and pulse duration are 1.2×10^{12} A/m^2 and 5 μs, respectively. DW is displaced from left to right by the pulsed current [77]

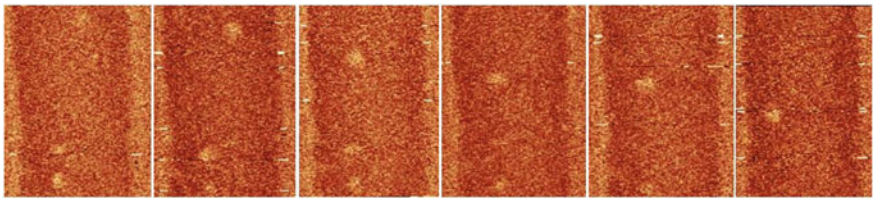

Fig. 8.22 Series of images showing magnetic skyrmions shift along the track between 3 ns, $j = 3.9 \times 10^{11}$ A/m^2 electric pulses. Scale bar is 500 nm

References

1. A. Hubert, R. Schäfer, *Magnetic Domains* (Springer, Berlin, 2000)
2. A. Tonomura, T. Matsuda, J. Endo, T. Arii, K. Mihama, Phys. Rev. Lett. **44**, 1430 (1980)
3. K. Koike, K. Hayakawa, Appl. Phys. Lett. **45**, 585 (1984)
4. M. Johnson, J. Clarke, J. Appl. Phys. **67**, 6141 (1990)
5. R. Wiesendanger, H.J. Güntherodt, G. Güntherodt, R.J. Gambino, R. Ruf, Phys. Rev. Lett. **65**, 247 (1990)
6. R. Allenspach, A. Bischof, Appl. Phys. Lett. **54**, 587 (1989)
7. S.N. Molotkov, Surf. Sci. **287–288**, 1098 (1993)
8. R. Laiho, H.J. Reittu, Surf. Sci. **289**, 363 (1993)
9. S.F. Alvarado, P. Renaud, Phys. Rev. Lett. **68**, 1387 (1992)
10. M.W.J. Prins, H. van Kempen, H. van Leuken, R.A. de Groot, W. van Roy, J. de Boeck, J. Phys.: Condens. Matter **7**, 9447 (1995)
11. S.M. Sze, *Physics of Semiconductor Devices*, 2nd edn. (Wiley, New York, 1981)
12. K. Sueoka, K. Mukasa, K. Hayakawa, Jpn. J. Appl. Phys. **32**, 2989 (1993)
13. Y. Suzuki, W. Nabhan, R. Shinohara, K. Yamaguchi, K. Mukasa, J. Magn. Magn. Mater. **198–199**, 540 (1999)
14. H. Kodama, T. Uzumaki, M. Oshiki, K. Sueoka, K. Mukasa, J. Appl. Phys. **83**, 6831 (1999)
15. A.M. Chang, H.D. Hallen, L. Harriot, H.F. Hess, H.L. Kao, R.E. Miller, R. Wolfe, J. van der Ziel, Appl. Phys. Lett. **61**, 1974 (1992)
16. T. Shono, T. Hasegwa, T. Fukumura, H. Ohno, Appl. Phys. Lett. **77**, 1363 (2000)
17. A. Sandhu, K. Kurosawa, M. Dede, A. Oral, Jpn. J. Appl. Phys. **43**, 2 (2004)
18. J. Gutierrez, B. Raes, A.V. Silhanek, L.J. Li, N.D. Zhigadlo, J. Karpinski, J. Tempere, V.V. Moshchalkov, Phys. Rev. B **85**, 094511 (2012)
19. J.R. Kirtley, M.B. Ketchen, K.G. Stawiasz, J.Z. Sun, W.J. Gallagher, S.H. Blanton, S.J. Wind, Appl. Phys. Lett. **66**, 1138 (1995)
20. M.B. Ketchen, T. Kopley, H. Ling, Appl. Phys. Lett. **44**, 1008 (1984)
21. D. Mailly, C. Chapelier, A. Benoit, Phys. Rev. Lett. **70**, 2020 (1993)
22. F. Grhhl, M. Mück, M. Kreutzbruck, J. Dechert, Rev. Sci. Instrum. **72**, 2090 (2001)
23. M.E. Huber, N.C. Koshnick, H. Bluhm, L.J. Archuleta, T. Azua, P.G. Björnsson, B.W. Gardner, S.T. Halloran, E.A. Lucero, K.A. Moler, Rev. Sci. Instrum. **79**, 053704 (2008)
24. J.R. Kirtley, L. Paulius, A.J. Rosenberg, J.C. Palmstrom, D. Schiessl, C.L. Jermain, J. Gibbons, C.M. Holland, Y. Fung, M.E. Huber, M.B. Ketchen, D.C. Ralph, G.W. Gibson Jr., K.A. Moler, Supersond. Sci. Technol. **29**, 124001 (2016)
25. E. Betzig, J.K. Trautman, R. Wolfe, E.M. Gyorgy, P.L. Finn, M.H. Kryder, C.-H. Chang, Appl. Phys. Lett. **61**, 142 (1992)
26. B. Hecht, H. Bielefeldt, Y. Inouye, D.W. Pohl, L. Novotny, J. Appl. Phys. **81**, 2492 (1997)
27. B. Hecht, B. Sick, U.P. Wild, V. Decert, R. Zenobi, O.J.F. Martin, D. Pohl, J. Chem. Phys. **112**, 7761 (2000)
28. U.Ch. Fischer, D.W. Pohl, *Phys. Rev. Lett.* **62**, 4 (1989)

29. T. Kalkbrenner, M. Ramstein, J. Mlynek, V. Sandoghdar, J. Microscopy **202**, 72 (2000)
30. J. Rudge, H. Xu, J. Kolthammer, Y.K. Hong, B.C. Choi, Rev. Sci. Instrum. **86**, 023703 (2015)
31. P.S. Keatley, T.H.J. Loughran, E. Hendry, W.L. Barnes, R.J. Hicken, J.R. Childress, J.A. Katin, *Rev. Sci. Instrum.* **88**, 123708 (2017)
32. G. Binnig, H. Rohrer, C. Gerber, E. Weibell, Phys. Rev. Lett. **49**, 57 (1982)
33. G. Binnig, C.F. Quate, C. Gerber, Phys. Rev. Lett. **56**, 930 (1986)
34. Y. Martin, C.C. Williams, H.K. Wickramasinghe, J. Appl. Phys. **61**, 4723 (1987)
35. J. Szymońska, F. Krok, Int. J. Bio. Macromol. **33**, 1 (2003)
36. Y. Martin, H.K. Wickramasinghe, Appl. Phys. Lett. **50**, 1445 (1987)
37. K. Sueoka, K. Okuda, N. Matsubara, F. Sai, J. Vac. Sci. Technol., B **9**, 1313 (1991)
38. D. Rugar, H.J. Mamin, P. Guethner, S.E. Lambert, J.E. Stern, I. McFadyen, T. Yogi, J. Appl. Phys. **68**, 1169 (1990)
39. Digital Instruments, *Support Note No. 229, Rev. B Magnetic Force Microscopy (MFM)* (Santa Barbara, USA, 1996)
40. H. Kaiju, H. Kasa, T. Komine, S. Mori, T. Misawa, T. Abe, J. Nishii, J. Appl. Phys. **117**, 17738 (2015)
41. A.J. den Boef, *Appl. Phys. Lett.* **56**, 2045 (1990); Z. Liu, Y. Dan, Q. Jinjun, Y. Wu, *J. Appl. Phys.* **91**, 8843 (2002)
42. G.N. Phillips, M. Siekman, L. Abelmann, J.C. Lodder, Appl. Phys. Lett. **81**, 865 (2002)
43. L. Gao, L.P. Yue, T. Yokota, R. Skomski, S.H. Liou, H. Saito, S. Ishio, IEEE Trans. Magn. **40**, 2194 (2004)
44. N. Amos, R. Ikkawai, R. Haddon, D. Litvinov, S. Khizroev, Appl. Phys. Lett. **93**, 3116 (2008)
45. T. Yamaoka, K. Watanabe, Y. Shirakawabe, K. Chinone, J. Magn. Soc. Jpn. **27**, 429 (2003)
46. K. Nagano, K. Tobari, K. Soneta, M. Ohtake, M. Futamoto, J. Magn. Soc. Jpn. **36**, 109 (2012)
47. Z. Liu, Y. Dan, Q. Jinjun, Y. Wu, *J. Appl. Phys.* **91**, 8843 (2002); G.N. Phillips, M. Siekman, L. Abelmann, J. C. Lodder, *Appl. Phys. Lett.* **81**, 865 (2002)
48. M.A. Al-Khafaji, W.M. Rainforth, M.R.J. Gibbs, J.E.L. Bishop, H.A. Davies, IEEE Trans. Magn. **32**, 4138 (1996)
49. T. Hasegawa, W. Pei, T. Wang, Y. Fu, T. Washiya, H. Saito, S. Ishio, Acta Mater. **56**, 1564 (2008)
50. T. Yamaoka, H. Tsujikawa, R. Hirose, A. Ito, H. Kawamura, T. Sakon, J. Magn. Soc. Jpn. **35**, 60 (2011)
51. H. Saito, H. Ikeya, G. Egawa, S. Ishio, S. Yoshimura, J. Appl. Phys. **105**, 07D524 (2009)
52. H. Katayama, S. Sawamura, Y. Ogimoto, J. Nakajima, K. Kojima, K. Ohta, J. Magn. Soc. Jpn. **23**, 233 (1999)
53. R.E. Rottmayer, S. Batra, D. Buechel, W.A. Challener, J. Hohlfeld, Y. Kubota, L. Li, B. Lu, C. Mihalcea, K. Mountfield, K. Pelhos, C. Peng, T. Rausch, M.A. Seigler, D. Weller, X.-M. Yang, IEEE Trans. Magn. **42**, 2417 (2006)
54. J.-G. Zhu, H. Zhu, Y. Tang, IEEE Trans. Magn. **44**, 125 (2008)
55. M.A. Seigler, W.A. Challener, E. Gage, N. Gokemeijer, G. Ju, B. Lu, K. Pelhos, C. Peng, R.E. Rottmayer, X. Yang, H. Zhou, T. Rausch, IEEE Trans. Magn. **44**, 119 (2008)
56. T. Raush, A.S. Chu, P. Lu, S. Puranam, D. Nagulapally, T. Lammers, J.W. Dykes, E.C. Gage, IEEE Trans. Magn. **51**, 4 (2015)
57. O. Fruchart, B. Dieny, M. Chshiev, B. Charles, N. Strelkov, A. Truong, A. Hallal, J. Wang, Y.K. Takahashi, T. Mizuno, K. Honi, IEEE Trans. Magn. **54**, 0800111 (2018)
58. J. Matlak, K. Komvopoulos, Sci. Rep. **8**, 9647 (2018)
59. T. Seki, K. Utsumiya, Y. Nozaki, H. Imamura, K. Takanashi, Nature Commun. **4**, 1726 (2013)
60. Y. Wang, Y. Tang, J. Zhu, J. Appl. Phys. **105**, 07B902 (2009)
61. J.-G. Zhu, Y. Wang, IEEE Trans. Magn. **46**, 751 (2010)
62. Y. Kanai, R. Itagaki, S.J. Greaves, H. Muraoka, IEEE Trans. Magn. **53**, 11 (2017)
63. B.D. Terris, T. Thomson, J. Phys. D Appl. Phys. **38**, R199 (2005)
64. C. Vogler, A. Abert, F. Bruckner, D. Suess, D. Praetorius, Appl. Phys. Lett. **108**, 102406 (2018)
65. Z. Meng, G. Li, H. Wong, S. Ng, S. Yiu, C. Ho, C. Leung, I. Manners, W. Wong, Nanoscale **9**, 731 (2017)

66. http://idema.org/?page_id=5868
67. I.L. Prejbeanu, S. Bandiera, J. Alvarez-Hérault, R.C. Sousa, B. Dieny, J.-P. Nozières, J. Phys. D Appl. Phys. **46**, 074002 (2013)
68. A. Hirohata, K. Takanashi, J. Phys. D Appl. Phys. **47**, 193001 (2014)
69. S. Yakata, H. Kubota, T. Seki, K. Yakushiji, A. Fukushima, S. Yuasa, K. Ando, IEEE Trans. Magn. **46**, 2232 (2010)
70. L. Tryputen, K.-H. Tu, S.K. Piotrowski, M. Bapna, S.A. Majetich, C. Sun, P.M. Voyles, H. Almasi, W. Wang, P. Vargas, J.S. Tresback, C.A. Ross, Nanotechnology **27**, 185302 (2016)
71. S. Chikazumi, *Physics of Ferromagnetism* (Oxford University Press, Oxford, 1997)
72. J. Slonczewski, J. Magn. Magn. Mater. **159**, L1 (1996)
73. L. Berger, Phys. Rev. B **54**, 9353 (1996)
74. J. Grollier, P. Boulenc, V. Cros, A. Hamzić, A. Vaurès, A. Fert, G. Faini, Appl. Phys. Lett. **83**, 509 (2003)
75. M. Tsoi, R.E. Fontana, S.S.P. Parkin, Appl. Phys. Lett. **83**, 2617 (2003)
76. A. Yamaguchi, T. Ono, S. Nasu, K. Miyake, K. Mibu, T. Shinjo, Phys. Rev. Lett. **92**, 077205 (2004)
77. M. Yamanouchi, D. Chiba, F. Matsukura, H. Ohno, Nature **428**, 539 (2004)
78. J.S. Gardner, J. Phys. Condens. Matter **23**, 160301 (2011)
79. U. Rössler, *Spin Waves: Magnons* (Springer, Berlin, 2009)
80. A. Hrabec, J. Sampaio, M. Belmeguenai, I. Gross, R. Weil, S.M. Chérif, A. Stashkevich, V. Jacques, A. Thiaville, S. Rohart, Nat. Commun. **8**, 15765 (2016)